






## Open Archive Toulouse Archive Ouverte (OATAO)

OATAO is an open access repository that collects the work of Toulouse researchers and makes it freely available over the web where possible

This is a Publisher's version published in: <http://oatao.univ-toulouse.fr/23688>

**Official URL:** <https://doi.org/10.1016/j.jma.2018.12.002>

### To cite this version:

Leleu, Samuel  and Rives, Bertrand and Caussé, Nicolas  and Pébère, Nadine  *Corrosion rate determination of rare-earth Mg alloys in a Na<sub>2</sub>SO<sub>4</sub> solution by electrochemical measurements and inductive coupled plasma-optical emission spectroscopy.* (2019) *Journal of Magnesium and Alloys*, 7 (1). 47-57.  
ISSN 2213-9567

Any correspondence concerning this service should be sent to the repository administrator: [tech-oatao@listes-diff.inp-toulouse.fr](mailto:tech-oatao@listes-diff.inp-toulouse.fr)

# Corrosion rate determination of rare-earth Mg alloys in a Na<sub>2</sub>SO<sub>4</sub> solution by electrochemical measurements and inductive coupled plasma-optical emission spectroscopy

Samuel Leleu<sup>a,b</sup>, Bertrand Rives<sup>b</sup>, Nicolas Causse<sup>a</sup>, Nadine Pébère<sup>a,\*</sup>

<sup>a</sup> CIRIMAT, Université de Toulouse, CNRS, INPT, UPS, ENSIACET, 4 allée Emile Monso BP44362, 31030 Toulouse cedex 4 France

<sup>b</sup> IRT Saint Exupéry, 118 route de Narbonne - CS 44248, 31432 Toulouse, France

Received 8 August 2018; received in revised form 22 November 2018; accepted 4 December 2018

Available online 12 January 2019

## Abstract

The corrosion resistance of three Mg alloys containing rare-earth elements (WE43, EV31 and ZE41) was studied and compared to that of two Mg–Al alloys (AZ31 and AZ91) and of pure Mg (99.95 wt.%). Current-voltage curves and electrochemical impedance measurements were performed with rotating disk electrodes in an aerated 0.1M Na<sub>2</sub>SO<sub>4</sub> solution. For all the alloys, it was confirmed that the intermetallic particles acted as local cathodes and that more protective films were formed on the alloys surface by comparison with the pure Mg. Corrosion rates were determined from inductive coupled plasma-optical emission spectroscopy measurements and from the electrochemical measurements. Higher corrosion rates were observed for the rare-earth Mg alloys compared to the AZ series alloys. These data allowed the corrosion mechanisms to be discussed.

© 2019 Published by Elsevier B.V. on behalf of Chongqing University.

This is an open access article under the CC BY-NC-ND license. (<http://creativecommons.org/licenses/by-nc-nd/4.0/>)

Peer review under responsibility of Chongqing University

**Keywords:** Magnesium alloys; Rare-earth elements; EIS; ICP-OES; Interface.

## 1. Introduction

Magnesium alloys represent alternative materials for many industries including transport, electronic devices, and biodegradable medical implants. Their use in automobile and aeronautic domains are more and more promising thanks to their low density (about 33% lower than that of aluminium alloys) and good mechanical properties. Nevertheless, use restrictions of Mg alloys still exist due to low ignition temperature and poor corrosion resistance. The addition of rare-earth elements improves their flammability resistance and commercial Mg alloys, such as the WE43, are designed to present high specific strength and good creep resistance, even at high temperature [1,2]. However, the high reactivity of magnesium alloys in aqueous environments remains the main drawback. In addition, the development of protective coatings is partially

limited by a lack of knowledge of the corrosion mechanisms on bare alloys and their behaviour in representative media.

Aluminium is one of the most common alloying element in Mg alloys [3]. The corrosion behaviour of AZ Mg alloys series (Mg–Al–Zn) have been extensively studied [4–14]. It is known that Al can have either a beneficial or a detrimental role on the corrosion resistance of Mg alloys depending on its concentration and on the morphology of the intermetallic  $\beta$ -phase (Mg<sub>17</sub>Al<sub>12</sub>) [4,5,10–14]. Studies on the influence of rare-earth (RE) elements on the corrosion resistance of Mg alloys are relatively scarce compared to those on the AZ Mg alloys. Corrosion studies on binary Mg alloys showed a decrease of the corrosion resistance with the addition of rare-earth elements such as Y, Ce, La or Nd [15,16]. On the other hand, Arrabal et al. concluded that addition of Nd to the AM50 or the AZ91 Mg alloys improved their corrosion resistance [17]. Takenaka et al. showed that the corrosion resistance of Mg was greatly improved by adding small amounts of RE (La, Nd, Ce), whereas the RE excess deteriorated the

\* Corresponding author.

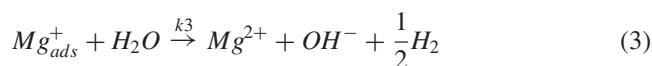
E-mail address: [nadine.pebere@ensiacet.fr](mailto:nadine.pebere@ensiacet.fr) (N. Pébère).

corrosion resistance [18]. Similarly, Luo et al. concluded that small amount of Y improved the corrosion resistance of the AZ91 alloy [19]. Among the Mg rare-earth commercial alloys, the Mg–Y–Nd–Zr (WE43) [20–25], the Mg–Gd–Nd–Zn (EV31) [26–28] and the Mg–Zn–Zr (ZE41) [23,29–31] are the most studied and used for industrial applications. For the ZE41 alloy immersed in a 0.001M NaCl solution, Neil et al. observed strong attacks linked to galvanic couplings between the matrix and Zr-rich particles and also between the matrix and secondary T-phase ( $Mg_7Zn_3RE$ ) that crystallizes along the grain boundaries [29]. Galvanic couplings were also observed between the matrix and rare-earth-rich grain boundaries in the case of the EZ33 alloy [32] and for a Mg–Y–Zr–RE alloy between the matrix and the Nd-rich second phase [33]. On the other hand, Pinto et al. [32] showed, from impedance results, that the WE54 alloy exhibited the highest impedance values which was attributed to the presence of yttrium amorphous oxide ( $Y_2O_3$ ). From X-ray photoelectron spectroscopy (XPS) and time-of-flight secondary ion mass spectroscopy (ToF-SIMS) analyses, Ardelean et al. also indicated, for the WE43 alloy, an enrichment of the inner Mg oxide layer by  $Y_2O_3 / Y(OH)_3$  and small amounts of  $MgH_2$ ,  $ZrO_2$  and  $Nd_2O_3$  [20]. They concluded that the presence of Zr, Y and Nd oxides can explain the lower corrosion current for the WE43 alloy compared to that of the pure Mg. In a recent study, we showed that the oxides film, formed in a  $Na_2SO_4$  solution, was about 35% thinner and more protective for a WE43 Mg alloy than that formed on pure Mg [25]. The incorporation of Y and to a less extent of Zr and Nd would be at the origin of the thinner and more stable oxides film in agreement with the increase of the Pilling-Bedworth ratio in the case of the WE43 alloy [25]. Some authors also found that Zr-rich precipitates, formed after heat-treatment, would confer better corrosion resistance to rare-earth Mg alloys which was explained by a barrier effect and higher stability of the oxide layer [20,21,32,33]. Thus, it appears that the corrosion of the rare-earth Mg alloys is governed by both the detrimental effect of the galvanic couplings between the matrix and the intermetallic particles and the beneficial role of these alloying elements on the passive film, particularly when they are present in the solid solution. The influence of these two antagonist effects on their corrosion rates is difficult to predict and corrosion rate determination from electrochemical measurements remains under discussion.

The corrosion rates of Mg and Mg alloys are usually estimated by one or multiple methods such as [34]: weight loss, quantity of  $Mg^{2+}$  released, hydrogen evolution and electrochemical techniques (polarization curves and electrochemical impedance measurements (EIS)). Several authors indicated that the corrosion rates estimated from the electrochemical methods are often underestimated compared to other techniques [14,35–38]. Song and Atrens concluded that the use of Tafel extrapolation or polarization resistance measurements for the determination of the corrosion current of pure Mg or Mg alloys was unsuitable due to the fact that several cathodic and anodic reactions are involved in the corrosion mechanism (existence of a partially protective film, particle undermining,

multi-step oxidation) [14]. For the determination of the corrosion rate, some authors also suggested that in the Stern-Geary equation, the use of the polarization resistance,  $R_p$ , determined at the zero frequency on the impedance diagrams instead of the charge transfer resistance,  $R_T$ , measured at intermediate frequency, was more appropriated and led to better agreement between electrochemical and non-electrochemical evaluations of the corrosion rates [38–40]. The determination of  $R_p$ , from the impedance diagrams, was often based on a fitting procedure that could lead to an erroneous determination of the  $R_p$  value due to a limited number of points in the low-frequency domain. The difficulty to measure the corrosion rates of Mg alloys results from the fact that the corrosion mechanisms are not totally understood despite large discussions. Today there is an important controversy on the corrosion mechanisms of pure Mg, especially the explanation of the anomalous phenomenon observed in the anodic range, called negative difference effect (NDE) that corresponds to an increase of the cathodic hydrogen evolution reaction with anodic overvoltage. Several explanations have been proposed; modern theories include:

- i) Increase of the cathodic hydrogen evolution reaction explained by an electrocatalytic effect which is called enhanced catalytic surface theory, one experimental example is the enrichment of the corrosion product film ( $MgO/Mg(OH)_2$ ) with more noble metal [41–47]. However, Fajardo et al. have recently concluded that the “enhanced electrocatalytic activity of the oxidized Mg surfaces” could only account for a small part of the NDE and that the latter is primarily governed by anodic dissolution [48].
- ii) Existence of an adsorbed intermediate species, such as  $Mg^+_{ads}$ , and its chemical reaction with water to produce dihydrogen following these series of reactions [49,50].



Corrosion mechanism of Mg is controlled by the existence of a thin and dense MgO layer that grows on the surface with immersion time, both free-film areas and the MgO layer are covered with a thick and porous  $Mg(OH)_2$  corrosion products (Eq. (4)–(5) [49–52].



Some recent papers suggested that the re-deposition of impurities, such as iron, in the corrosion products layer might

Table 1

Chemical compositions (wt. %) of the Mg alloys in accordance with ASTM B951-11, other rare earths (ORE) shall principally be (a) Gd, Dy, Er, Yb, (b) Ce, La, Pr, (c) Ce, La, Nd, Pr.

Materials	Al	Mn	Gd	Li	Y	Nd	Zn	Zr	ORE	Mg
AZ31B-O	2.5 - 3.5	0.20 - 1.0	–	–	–	–	0.6 - 1.4	–	–	Bal.
AZ91D-T6	8.3 - 9.7	0.15 - 0.50	–	–	–	–	0.35 - 1.0	–	–	Bal.
EV31A-T6	–	–	1.0 - 1.7	–	–	2.6 - 3.1	0.20 - 0.50	0.30 - 1.0	0.40 <sup>a</sup>	Bal.
WE43A-T6	–	–	–	0.20	3.7 - 4.3	2.0 - 2.5	0.20	0.40 - 1.0	1.9 <sup>b</sup>	Bal.
ZE41A-T5	–	–	–	–	–	–	3.5 - 5.0	0.40 - 1.0	0.75 - 1.7 <sup>c</sup>	Bal.

not be sufficient to fully explain the NDE [53,54]. Although there is no experimental proof of the existence of an adsorbed species, such as  $(\text{Mg}^+)_{\text{ads}}$  [55], the relaxation process of adsorbed species could explain the presence of the inductive loop observed on the impedance diagrams of pure Mg and Mg alloys [19,32,38–40] and the NDE mechanism [50]. The chemical reaction which could be at the origin of the NDE (reaction 3) does not contribute to the electrochemical response. Thus, the estimation of the corrosion rates from the electrochemical techniques will ever be underestimated [30,35,36]. Additionally, the existence of an “undermining effect” that consists in the falling out of a particle due to galvanic couplings could also contribute to an underestimation of the corrosion rates when determined by electrochemical measurements [5].

The aim of the present work was to study and to compare the corrosion resistance of commercial Mg alloys in a  $\text{Na}_2\text{SO}_4$  solution. Three rare-earth Mg alloys (EV31, WE43 and ZE41) and two AZ Mg alloys (AZ31 and AZ91) were chosen. Commercially pure Mg was used as the reference system. Current-voltage curves and electrochemical impedance measurements were performed with rotating disk electrodes in an aerated 0.1M  $\text{Na}_2\text{SO}_4$  solution. The corrosion rates were determined from the electrochemical results and compared to those obtained from the quantitative analysis of  $\text{Mg}^{2+}$  ions in solution by ICP-OES measurements, as an independent non-electrochemical technique. From these data, the objective of the work was to contribute to impedance data analysis in order to have a better understanding of the corrosion mechanisms, particularly for the rare-earth Mg alloys.

## 2. Experimental

### 2.1. Materials

The magnesium alloys were provided by Prodem-Bonnans Company. Their compositions are reported in Table 1. Thermal treatments are given according to ASTM B296-03. The wrought AZ31B alloy was in “O” condition (annealed and recrystallized) and the ZE41 alloy was in “T5” condition (artificially aged). The others Mg alloys were in “T6” condition (solution heat treated and then artificially aged).

For the electrochemical measurements, the working electrodes were rotating disks exposing a surface area of  $1 \text{ cm}^2$  consisting of the cross-section of cylindrical rods. Each Mg alloy sample was machined from wrought or casted ingots. For comparison, some electrochemical tests were performed

on pure commercial magnesium, purchased from Alfa Aesar with a purity of 99.95% (Fe: 250ppm; Al: 20ppm; Cu: 20ppm and Mn: 46ppm). The body of the rods was covered with a heat-shrinkable sheath, leaving only the tip of the rod in contact with the solution. The samples were abraded with successive SiC papers (grade P4000), cleaned with ethanol in an ultrasonic bath and finally dried in warm air.

The corrosive medium was prepared from deionized water by adding 0.1M  $\text{Na}_2\text{SO}_4$  (analytical grade VWR Chemicals reagents (AnalaR NORMAPUR)).

### 2.2. Microstructural characterization

The microstructure of the samples was characterized by scanning electron microscopy (SEM) with a LEO 435VP apparatus. Prior to the observations, the samples surface was abraded with successive SiC papers (grade 4000), diamond pastes and  $\text{SiO}_2$  colloidal suspension (Struers OP-S  $0.04 \mu\text{m}$ ). Then, they were etched during about 10–20s in a solution composed of 20mL acetic acid + 1mL nitric acid + 60mL ethylene glycol + 20mL distilled water. The acids were purchased from VWR Chemicals and the ethylene glycol from PanReac Applichem.

### 2.3. Electrochemical measurements

A classical three-electrode cell was used with a platinum grid auxiliary electrode, a saturated sulphate reference electrode (MSE) and the rod of Mg alloys or pure Mg sample as rotating disk electrode (RDE). It was checked that the electrochemical results were not influenced by the electrode rotation rate. However, without rotation the results were different from those obtained with the electrode rotation. The corrosion rates would be significantly lower in static conditions. This can be attributed to the accumulation of  $\text{OH}^-$  species at the metal/solution interface [56]. The use of the RDE allows an accurate control of the hydrodynamic regime at the electrode/electrolyte interface and thus a good reproducibility. With the RDE, the impedance diagrams, were obtained without dispersion until 3 mHz. The rotation rate was fixed at 250rpm.

Current-voltage curves were obtained using a Solartron 1287 electrochemical interface. They were plotted consecutively from the cathodic to the anodic range (from  $-0.5 \text{ V}$  to  $+0.5 \text{ V}$  vs. the corrosion potential ( $E_{\text{corr}}$ ) after a preliminary hold time of 24h at  $E_{\text{corr}}$ . The potential sweep rate

was fixed at  $10 \text{ mV min}^{-1}$ . The polarization curves were corrected from the ohmic drop, experimentally determined from the high-frequency limit of the impedance diagrams.

Electrochemical impedance measurements were carried out using a Solartron 1287 electrochemical interface connected to a Solartron 1250 frequency response analyzer. Impedance diagrams were obtained under potentiostatic regulation, at  $E_{corr}$ , over a frequency range of 65 kHz to a few mHz with 8 points per decade, using a  $30 \text{ mV}_{\text{rms}}$  sinusoidal voltage. The linearity of the system was checked by varying the amplitude of the ac signal applied to the sample. Under galvanostatic regulation, the impedance diagrams were similar to those obtained in potentiostatic mode. The spectra obtained were always consistent with the Kramers-Kronig relations [57]. At least two experiments were performed.

#### 2.4. ICP-OES analyses

Quantitative analysis of dissolved magnesium in the electrolytic solution was assayed by ICP-OES with a Thermo Scientific iCAP 6300 Spectrometer. The theoretical detection limit is 20 ppb. The calibration was performed between 0.5 and 20 ppm for Mg ions, which corresponds to the measured concentrations range. The experiments were carried out in similar conditions as those used for the electrochemical measurements. The cell was filled with 300 mL of a  $\text{Na}_2\text{SO}_4$  solution. Then, 10 mL of the solution was removed after 6 h, 24 h and 48 h of immersion for each Mg alloy and for pure Mg. The  $\text{Mg}^{2+}$  ions in the as-prepared  $\text{Na}_2\text{SO}_4$  solution was negligible. The contents in some elements, such as Al, Zn, Mn, Nd, Y and Zr, in the  $\text{Na}_2\text{SO}_4$  solution after immersion of the samples were also measured but they were considered negligible (lower than 0.1 ppm). The quantity of  $\text{Mg}^{2+}$  ions precipitated in the oxides/hydroxides film was not taken into account due to the experimental procedure and the error introduced by neglecting these  $\text{Mg}^{2+}$  ions was included in the reproducibility of the experiments.

#### 2.5. Determination of the corrosion rates from ICP-OES results and from electrochemical impedance data

The corrosion rates (CR), in  $\text{mm y}^{-1}$ , were calculated from the ICP-OES results (quantity of released  $\text{Mg}^{2+}$ ) by using the following relationship:

$$CR = 8.76 \cdot 10^4 \frac{CV}{S t_{imm} \rho} \quad (1)$$

$C$  is the  $\text{Mg}^{2+}$  concentration ( $\text{g l}^{-1}$ ),  $V$  is the volume of the electrochemical cell in l and  $t_{imm}$  is the immersion time (s).

The instantaneous corrosion current densities ( $i_{corr}$ ) were calculated by using the Stern-Geary relationship [58]:

$$i_{corr} = \frac{b_a b_c}{2.303(b_a + |b_c|)R_T} = \frac{B}{R_T} \quad (2)$$

where  $b_a$  and  $b_c$  are the anodic and cathodic Tafel slopes, respectively.  $R_T$  is the charge transfer resistance, extracted from

the diameter of the first capacitive loop on the impedance diagrams after 24 h of immersion. Thus:

$$B = \frac{b_a b_c}{2.303(b_a + |b_c|)} \quad (3)$$

For comparison, the instantaneous corrosion current densities were determined from the cathodic Tafel extrapolation at the corrosion potential.

Average corrosion rates ( $i_{corr,mean}$ ) were also calculated by integrating the  $R_T$  values obtained for different immersion times over 24 h.  $R_{T,mean}$  was calculated according to Eq. (4):

$$R_{T,mean} = \frac{1}{t_2 - t_1} \int_{t_1}^{t_2} R_T dt \quad (4)$$

where  $t_1$  and  $t_2$  correspond to 0 h and 24 h, respectively. Thus,  $i_{corr,mean}$  can be calculated:

$$i_{corr,mean} = \frac{b_a b_c}{2.303(b_a + |b_c|)R_{T,mean}} = \frac{B}{R_{T,mean}} \quad (5)$$

Afterwards,  $i_{corr,mean}$  (in  $\text{A cm}^{-2}$ ) was converted in corrosion rate  $CR$  (in  $\text{mm y}^{-1}$ ) with the Faraday's law:

$$CR = 3.15 \cdot 10^8 \frac{M}{n F \rho S} i_{corr,mean} \quad (6)$$

where  $n$  is the number of electrons transferred ( $n=2$ ),  $F$  is the Faraday's constant ( $96,485 \text{ C mol}^{-1}$ ),  $M$  is the molar mass of magnesium ( $24.3 \text{ g mol}^{-1}$ ),  $\rho$  is the density of the Mg alloy or of the pure Mg ( $\text{g cm}^{-3}$ ) and  $S=1 \text{ cm}^2$ .

### 3. Results

#### 3.1. Microstructure of the Mg alloys

SEM micrographs of the Mg alloys are presented in Fig. 1. The identification of the intermetallic phases was partly based on energy dispersive X-ray spectroscopy (EDX) analysis and on literature data. For the AZ91 Mg alloy, a large part of the surface area is covered by the  $\beta$ -phase ( $\text{Mg}_{17}\text{Al}_{12}$  particles) which forms a dense network in the  $\alpha$ -matrix [5]. Some Mg–Al–Zn intermetallic particles are also observed. The AZ31 Mg alloy displays the same type of intermetallic particles than the AZ91 alloy but the surface coverage is smaller due to a lower Al content. The WE43 and the EV31 Mg alloys microstructures are more complex due to the presence of fine clusters of secondary phases. The WE43 alloy presents small Y and Zr rich-precipitates in the grain and along the grain boundaries. The whitish “clouds” are enriched in Zr and slightly depleted in Mg, Y and Nd by comparison with the matrix [25]. In the EV31 Mg alloy, a large intermetallic phase composed of Mg, Nd and Gd is observed along the grains boundaries. This phase is known as  $\text{Mg}_{12}(\text{Nd}_x\text{Gd}_{1-x})$  [59] or  $\text{Mg}_3(\text{Nd,Gd})$  [60,61]. The whitish halos in the micrograph are attributed to Zr and Zn fine scale precipitates clusters [59]. For the ZE41 Mg alloy, an intermetallic phase that crystallizes along the grain boundaries can be clearly observed. This phase is known as T-phase ( $\text{Mg}_7\text{Zn}_3\text{RE}$ ) [23]. Smaller precipitates are also observed and, according to the literature, have been identified

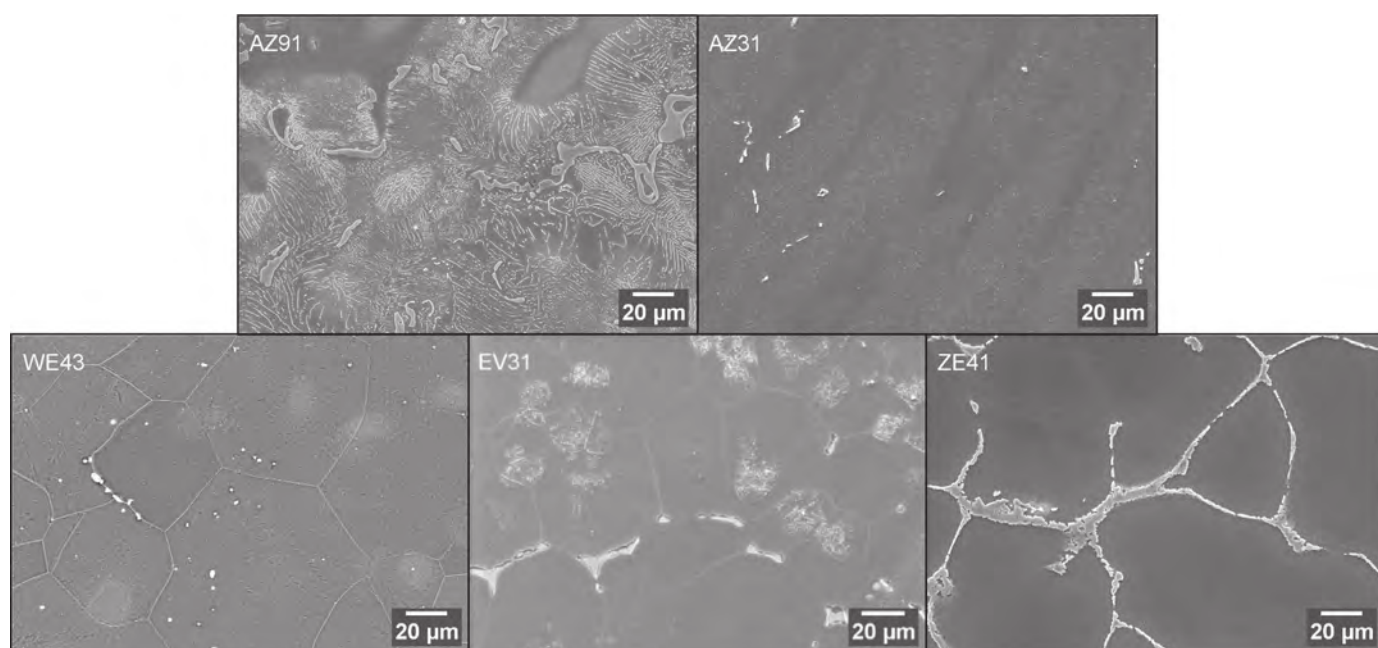


Fig. 1. SEM micrographs of the Mg alloys after polishing and chemical etching.

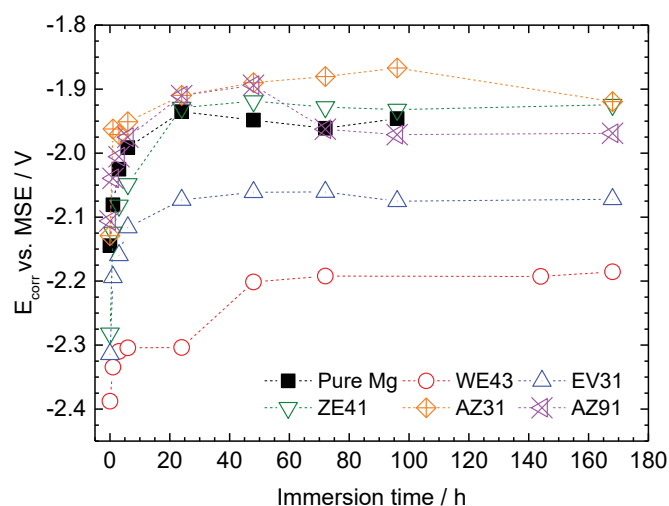


Fig. 2. Corrosion potential ( $E_{corr}$ ) of the different Mg alloys and of the pure Mg as function of time in a 0.1M  $\text{Na}_2\text{SO}_4$  solution.

as  $\text{Zr}_4\text{Zn}$  particles [23]. It can be underlined that Zn is the main alloying element in the ZE41 alloy and its RE content is low by comparison with the WE43 and the EV31 alloys.

### 3.2. Electrochemical results

#### 3.2.1. DC measurements

Fig. 2 illustrates the variation of  $E_{corr}$  of the pure Mg and of the five Mg alloys during immersion in a 0.1M  $\text{Na}_2\text{SO}_4$  solution. For all the alloys and for pure Mg,  $E_{corr}$  increases significantly at the beginning of immersion and then, progressively, it stabilizes after about 24h of immersion. The time required to reach the stationary state is relatively long (one day) which is in agreement with different works reported in

the literature [62]. The variation of  $E_{corr}$  with time for Mg and Mg alloys has been attributed to the development of a partially protective film composed of  $\text{MgO}/\text{Mg}(\text{OH})_2$  on the samples surface [51–53]. This change in  $E_{corr}$  was accompanied by an increase in pH of the electrolyte, from 6.5 at the beginning of immersion to a value of about 10 after some hours of immersion (10h–12h). According to the literature, the maximum of  $E_{corr}$  corresponds to the onset of stabilization of the pH value around 10.5 [62]. After 24h and beyond this immersion time, the  $E_{corr}$  values are slightly more anodic for the AZ31, the AZ91 and the ZE41 alloys than for the pure Mg ( $E_{corr}$  for pure Mg =  $-1.95$  V/MSE). For the AZ91 alloy, the drop of  $E_{corr}$  observed at 72h of immersion was related to an undermining effect linked to its microstructure. For the rare-earth rich alloys (WE43 and EV31), a significant cathodic shift of  $E_{corr}$  is observed. When a stationary state is reached, the  $E_{corr}$  values are about 150mV and 250mV more cathodic for the EV31 and the WE43, respectively compared to the pure Mg. From the work of Südholz et al. [63], if it is considered that most of the intermetallic particles in the Mg alloys act as local cathode, thus, the  $E_{corr}$  values for the Mg alloys should be shifted in the anodic direction. Thus, the shift of  $E_{corr}$  towards more negative values for these two alloys, in agreement with previous studies, can be attributed to the presence of the rare-earth elements in the Mg matrix, especially Zr [3,19,64].

Fig. 3 shows the polarization curves for the Mg alloys and for the pure Mg, corrected from the ohmic-drop. The cathodic branches present relatively similar slopes. In the anodic range, short linear parts can be observed before an inflexion point, generally attributed to the breakdown of the protective oxides film formed on the metal surface [25,49,65]. This breakdown potential is clearly visible for almost all the alloys except for the ZE41 alloy and for the pure Mg where the breakdown

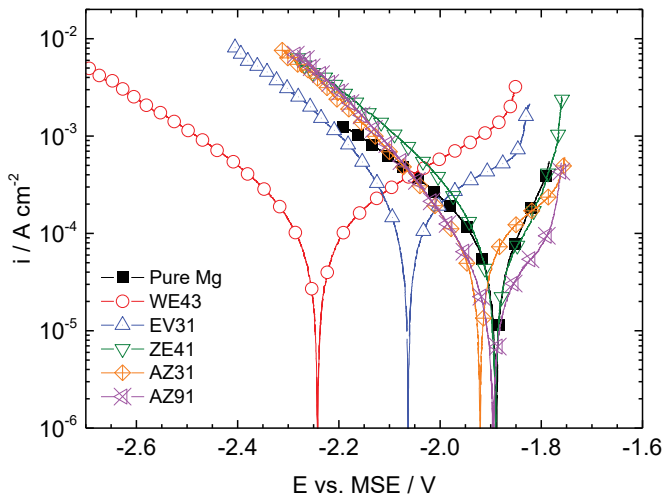


Fig. 3. Polarization curves obtained for the different Mg alloys and for the pure Mg after 24h of immersion at  $E_{corr}$  in a 0.1M  $\text{Na}_2\text{SO}_4$  solution. The curves were corrected from the ohmic drop.

Table 2

Cathodic ( $b_c$ ) and anodic ( $b_a$ ) Tafel slopes graphically determined for the different Mg alloys and for pure Mg (from Fig. 3), after 24h of immersion in a 0.1  $\text{Na}_2\text{SO}_4$  solution ( $\Omega=250\text{rpm}$ ).  $B$  was calculated according to Eq. (3).

Materials	$-b_c$ (mV $\text{dec}^{-1}$ )	$b_a$ (mV $\text{dec}^{-1}$ )	$B$ (mV)
Mg	$265 \pm 10$	$120 \pm 10$	$36 \pm 2$
WE43	$275 \pm 10$	$318 \pm 10$	$64 \pm 2$
EV31	$250 \pm 10$	$323 \pm 10$	$61 \pm 2$
ZE41	$215 \pm 10$	$105 \pm 10$	$31 \pm 2$
AZ31	$170 \pm 10$	$220 \pm 10$	$42 \pm 2$
AZ91	$170 \pm 10$	$155 \pm 10$	$35 \pm 2$

potential is close to  $E_{corr}$ . For the two rare-earth Mg alloys (WE43 and EV31), the linear part in the anodic domain is more extended than for the other alloys. The Tafel slopes were graphically determined from the curves presented in Fig. 3. The anodic slopes were measured in a potential range from  $E_{corr}$  to the breakdown potential for all the alloys. For the pure Mg and for the ZE41, the determination of  $b_a$  was not accurate due to the fact that  $E_{corr}$  is close to the breakdown potential. The  $b_a$ ,  $b_c$ , and  $B$  coefficient values are reported in Table 2. The  $b_c$  values are lower for the Mg–Al alloys, around  $170\text{mV dec}^{-1}$ . A  $b_c$  value of about  $250\text{mV dec}^{-1}$  was determined for the ZE41, the EV31, the WE43 and for the pure Mg. In contrast, the  $b_a$  values are significantly dependent on the alloy. For the WE43 and the EV31, the values of  $b_a$  (around  $320\text{mV dec}^{-1}$ ) are about three times higher than those measured for the ZE41 and for the pure Mg. For the AZ31 and the AZ91, the  $b_a$  values are in between those obtained for the other alloys. Thus, the  $B$  values (Eq. (3)) are around  $36\text{mV}$  for the pure Mg, the ZE41, the AZ31 and the AZ91 and around  $65\text{mV}$  for the WE43 and the EV31. The value of  $B$  generally reported in the literature is in the order of  $35\text{mV}$  [36,38,39].

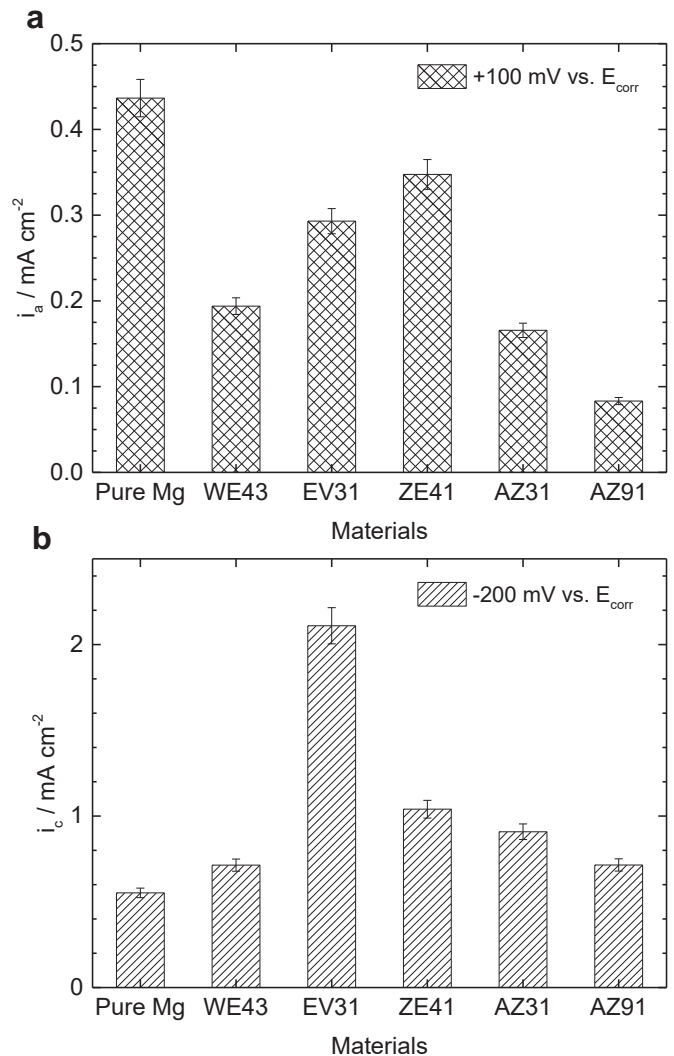


Fig. 4. (a) Anodic current densities at  $+100\text{mV vs. }E_{corr}$  and (b) cathodic current densities at  $-200\text{mV vs. }E_{corr}$  for the different Mg alloys and for the pure Mg after 24h of immersion in a 0.1M  $\text{Na}_2\text{SO}_4$  solution. The current densities were extracted from the polarization curves (Fig. 3).

To compare the anodic and cathodic behaviours of the alloys with that of the pure Mg, the current densities were taken from the polarization curves (Fig. 3) for two overvoltages: one in the anodic range at  $+100\text{mV vs. }E_{corr}$  (just before the breakdown potential), and one in the cathodic range at  $-200\text{mV vs. }E_{corr}$ . The data are shown in Fig. 4a and b for the anodic and cathodic domains, respectively. In Fig. 4a, it can be seen that the anodic current densities ( $i_a$ ) are in the same order of magnitude, independently of the material. However,  $i_a$  is the highest for the pure Mg, followed by the ZE41, the EV31 and then, the WE43 with  $i_a$  close to that measured for the AZ31 and finally the AZ91 with the lowest  $i_a$  value. This result confirmed that the films formed on the alloys surface are more protective than the one formed on the pure Mg [4–14,20–33]. The lower anodic current densities measured for the Mg–Al alloys (AZ91 and AZ31) can be explained by the incorporation of Al in the Mg oxide layer [66]. In Fig. 4b,

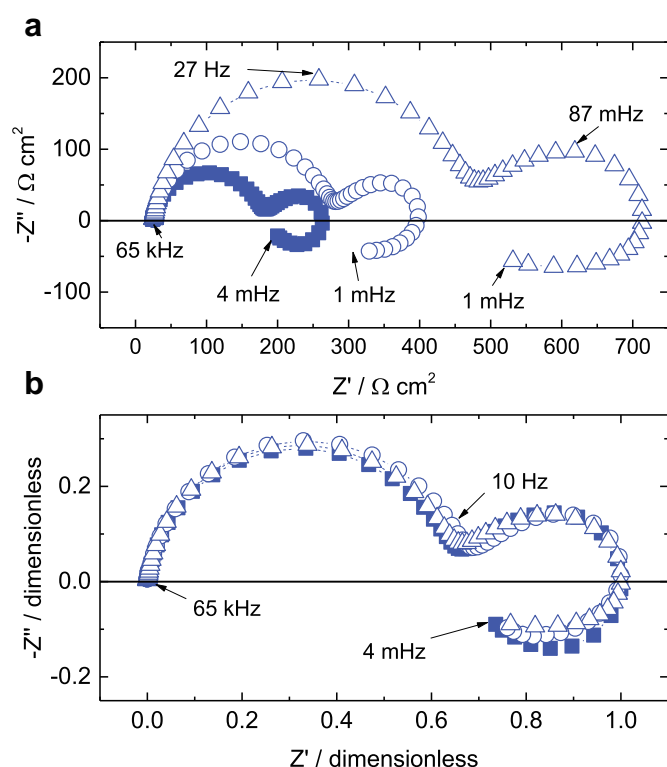


Fig. 5. (a) Electrochemical impedance diagrams of the EV31 Mg alloy obtained after different hold times at  $E_{corr}$  in a 0.1M  $\text{Na}_2\text{SO}_4$  solution: (■) 6h, (○) 24h, (△) 168h. (b) Normalized impedance diagrams.

in contrast to the anodic domain, it can be observed that all the alloys exhibit higher cathodic current densities ( $i_c$ ) than those measured for the pure Mg. This result shows that water reduction kinetics is increased in the case of the alloys. At  $-200\text{ mV}$  vs.  $E_{corr}$ , the  $i_c$  values are significantly high for the EV31 (four times higher than the values obtained for the pure Mg); values in the same order of magnitude are measured for the ZE41 and the AZ31. The lowest  $i_c$  values were obtained for the AZ91 and the WE43. The significant increase of the cathodic current densities can be explained by the presence of the intermetallic particles which act as local cathodes, in agreement with literature data [29,32].

From the polarization curves, it can be seen that the presence of alloying elements (Al, Zn, Y, Nd, Zr, Gd) influenced the anodic and cathodic behaviours of the Mg alloys: as a general feature, the cathodic currents increased and the anodic ones decreased by comparison with those obtained on pure Mg (Fig. 4). Thus, from a point of view of their corrosion resistance, the significant increase of the cathodic currents, attributed to the galvanic coupling between the intermetallic particles and the matrix will be particularly detrimental and the slight decrease of the anodic currents would not be sufficient to counterbalance the cathodic reaction on the intermetallic particles.

### 3.2.2. Electrochemical impedance measurements

As an example, Fig. 5a shows the impedance diagrams obtained at  $E_{corr}$  for the EV31 alloy for three immersion times

in 0.1M  $\text{Na}_2\text{SO}_4$ . The diagrams are characterized by the presence of three time constants. When the immersion time increases, the size of the three loops increases. The shape of the diagrams is similar to that obtained for pure magnesium. According to the work of Baril et al., the high-frequency capacitive loop results from the charge transfer resistance ( $R_T$ ), associated with reactions (1) and (2) which produce  $\text{Mg}^{2+}$  and to the oxide film capacitance ( $C_f$ ) [50]. The Mg dissolution occurs in free-film area. The oxide film resistance ( $R_f$ ) is assumed to be high (very protective) compared to the charge transfer resistance and thus  $R_f$  is not measured on the impedance diagrams. Moreover, the free-film area are small compared to the surface covered by the oxide film and, as a consequence, the double-layer capacitance ( $C_{dl}$ ) value, which is generally about  $50\text{--}100\ \mu\text{F cm}^{-2}$ , can be neglected with respect to  $C_f$ . The second time constant at mid frequencies corresponds to the diffusion of  $\text{Mg}^{2+}$  ions, produced at the interface, through the porous oxide/hydroxide layer and the inductive one, at low frequency, would be ascribed to the existence of relaxation process of adsorbed species [21,38,50]. In Fig. 5b, as previously done for the pure Mg [50], the impedance diagrams plotted for the three immersion times in Fig. 5a are normalized (the real and imaginary parts of the diagrams were divided by the maximum value of the real part of the impedance for each diagram). It can be seen that the three normalized diagrams are merged into a single diagram. This result indicates that the corrosion mechanism for the EV31 Mg alloy is controlled by the dissolution of the Mg matrix and is independent of the immersion time. The increase in size of the impedance diagrams with immersion time (Fig. 5a) can be simply attributed to a decrease of the active surface area due to the progressive surface coverage by the oxide film [25,50]. The same conclusions were drawn for all the alloys.

In Fig. 6a, the impedance diagrams obtained for the different Mg alloys and for the pure Mg are compared after 24h of immersion in the  $\text{Na}_2\text{SO}_4$  solution. All the diagrams present the same shape with the presence of the three time constants. Three groups can be seen: the pure Mg, the EV31 and the ZE41 alloys have the smallest comparable impedances; then, the WE43 and the AZ31 alloys with similar impedances, about twice higher than the previous one; and alone, the AZ91 alloy with the highest impedance (about four times higher than that of pure Mg). In the present work, equivalent circuits were not used to extract impedance parameters because the diffusion process of  $\text{Mg}^{2+}$  ions and the presence of adsorbed intermediates cannot be simply modelled by resistances, inductances and capacitances. The charge transfer resistance,  $R_T$ , was graphically determined from the diameter of the first capacitive loop for each alloy and for the pure Mg. These values will be used further to calculate the corrosion current densities (Eq. (2)). Fig. 6b shows the variation of  $R_T$  vs immersion time in 0.1M  $\text{Na}_2\text{SO}_4$  between 1h and 168h. Independently of the materials,  $R_T$  increases rapidly during the first hours of immersion, in agreement with the variation of  $E_{corr}$  (Fig. 2). After about 24h of immersion, a stationary  $R_T$  value is reached for the pure Mg but for all the alloys,



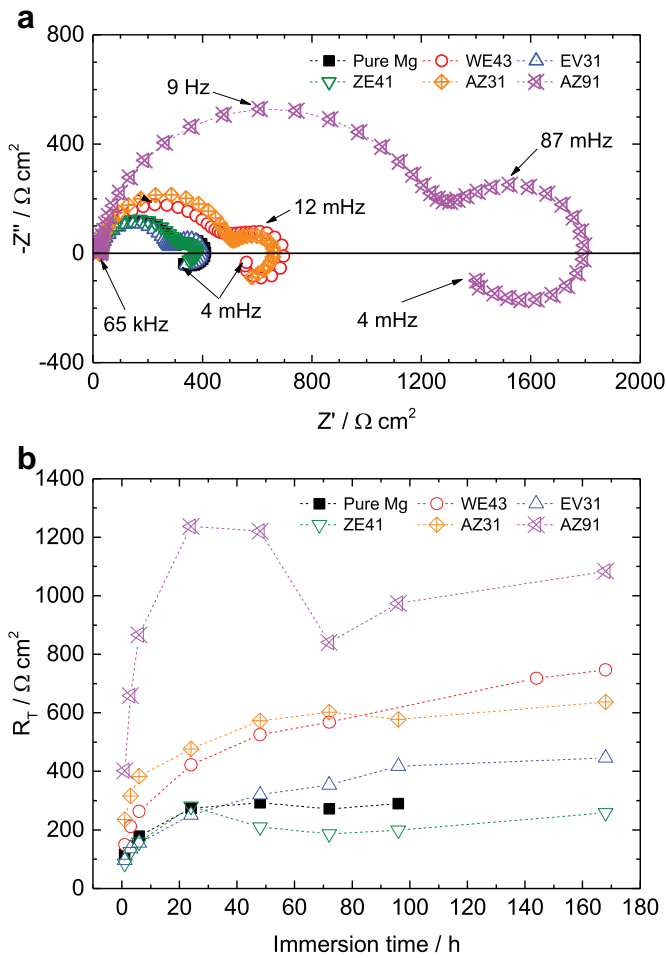


Fig. 6. (a) Electrochemical impedance diagrams obtained for the Mg alloys and for the pure Mg after 24 h of immersion in a 0.1 M  $\text{Na}_2\text{SO}_4$  solution; (b) Charge transfer resistance ( $R_T$ ) versus immersion time in a 0.1 M  $\text{Na}_2\text{SO}_4$  solution for the different Mg alloys and for the pure Mg.

$R_T$  continues to increase, particularly for the WE43 and the EV31. These variations account for the formation of protective films which progressively decreased the active surface area and become more protective due to the incorporation of alloying elements [25]. For the AZ91, the decrease of  $R_T$  observed at 72 h is attributed to the undermining effect [5]. After the experiment, the undermined particles were visible as holes on the electrode surface. This phenomenon led to an increase of the surface area and caused a decrease of the size of the loops in the impedance diagram and thus, a drop of the  $R_T$  value. It can be noted that even after 168 h of immersion, the  $R_T$  value ( $1100 \Omega \text{ cm}^2$ ) remains lower than that measured after 24 h of immersion ( $1240 \Omega \text{ cm}^2$ ). This would indicate a significant increase of the electrode surface area due to the undermining effect.

Impedance diagrams were also obtained for short immersion times (between 5 min and 55 min) in a limited frequency range to explore the behaviour of the alloys in relation with their microstructure. The diagrams obtained for the pure Mg and the EV31 Mg alloy are reported in Fig. 7a and b, respectively. The variation of  $R_T$  during the first hour of immersion

is reported in Fig. 7c for the two rare-earth Mg alloys (WE43 and EV31) and for the pure Mg. The variation of  $R_T$  for the other alloys (AZ series and ZE41) was similar to that of pure Mg and is not shown for the sake of clarity. For short immersion times, the shape of the diagrams is always the same and the inductive loop is clearly visible. For the pure Mg,  $R_T$  increases progressively and accounts for the formation of a protective film on the Mg surface, as already discussed for longer immersion times. For the two rare-earth Mg alloys, a non-monotonous variation is observed with a decrease and then an increase of  $R_T$ . For the EV31, this behaviour is more pronounced and the  $R_T$  values are low during the first hour of immersion. It was seen that the highest cathodic current densities were measured for this alloy (Fig. 4b). Thus, it can be assumed that at the beginning of immersion in the  $\text{Na}_2\text{SO}_4$  solution, the galvanic couplings due to the presence of numerous intermetallic phases can generate an increase of the active surface area. The undermining of some particles can be also possible, as observed for the AZ91 alloy. Thus, the decrease of  $R_T$  might be linked to an increase of the active surface area ( $>1 \text{ cm}^2$ ).

### 3.3. Determination of the corrosion rates by ICP-OES and comparison with the electrochemical data

The corrosion rates were calculated (Eq. (1)) from the quantitative analysis (ICP-OES measurements) of the  $\text{Mg}^{2+}$  ions in the  $\text{Na}_2\text{SO}_4$  solution for three immersion times: 6 h, 24 h and 48 h and the results are shown in Fig. 8. After 6 h of immersion, by comparison with the pure Mg, the corrosion rate is higher for the WE43 (about  $12 \text{ mm y}^{-1}$ ), similar for the ZE41 and the EV31 (around  $9 \text{ mm y}^{-1}$ ), lower for the AZ31 ( $5 \text{ mm y}^{-1}$ ) and the AZ91 ( $2.5 \text{ mm y}^{-1}$ ). For all the materials, the corrosion rates decrease with increasing immersion time in agreement with the electrochemical results. After 24 h and 48 h of immersion, the corrosion rates of the EV31 and WE43 alloys are always higher than that obtained for the pure Mg and lower for the other alloys (ZE41, AZ31 and AZ91). From the ICP-OES results, it can be concluded that the two rare-earth Mg alloys presented lower corrosion resistance in  $\text{Na}_2\text{SO}_4$  solution than the three other alloys. The corrosion rates ranking, in decreasing order, after 24 h of immersion, is:

$$\text{WE43} \sim \text{EV31} \sim \text{Pure Mg} > \text{ZE41} > \text{AZ31} > \text{AZ91}$$

It is noteworthy that this ranking from the ICP-OES measurements perfectly reflected the cathodic current densities recorded at  $-200 \text{ mV vs. } E_{\text{corr}}$  for the Mg alloys and for the pure Mg (Fig. 4b). This observation might be indicative that the corrosion rate is strongly connected to the cathodic process, due to the intermetallic particles reactivity. Thus, it seemed relevant to compare the instantaneous corrosion rate ( $i_{\text{corr}}$ ) determined from the cathodic Tafel extrapolation at  $E_{\text{corr}}$  (Fig. 3) and from the Stern-Geary relationship, using the  $B$  values (Table 2) and  $R_T$  graphically determined (Fig. 6b). The comparison of the  $i_{\text{corr}}$  values is shown in Fig. 9 and it

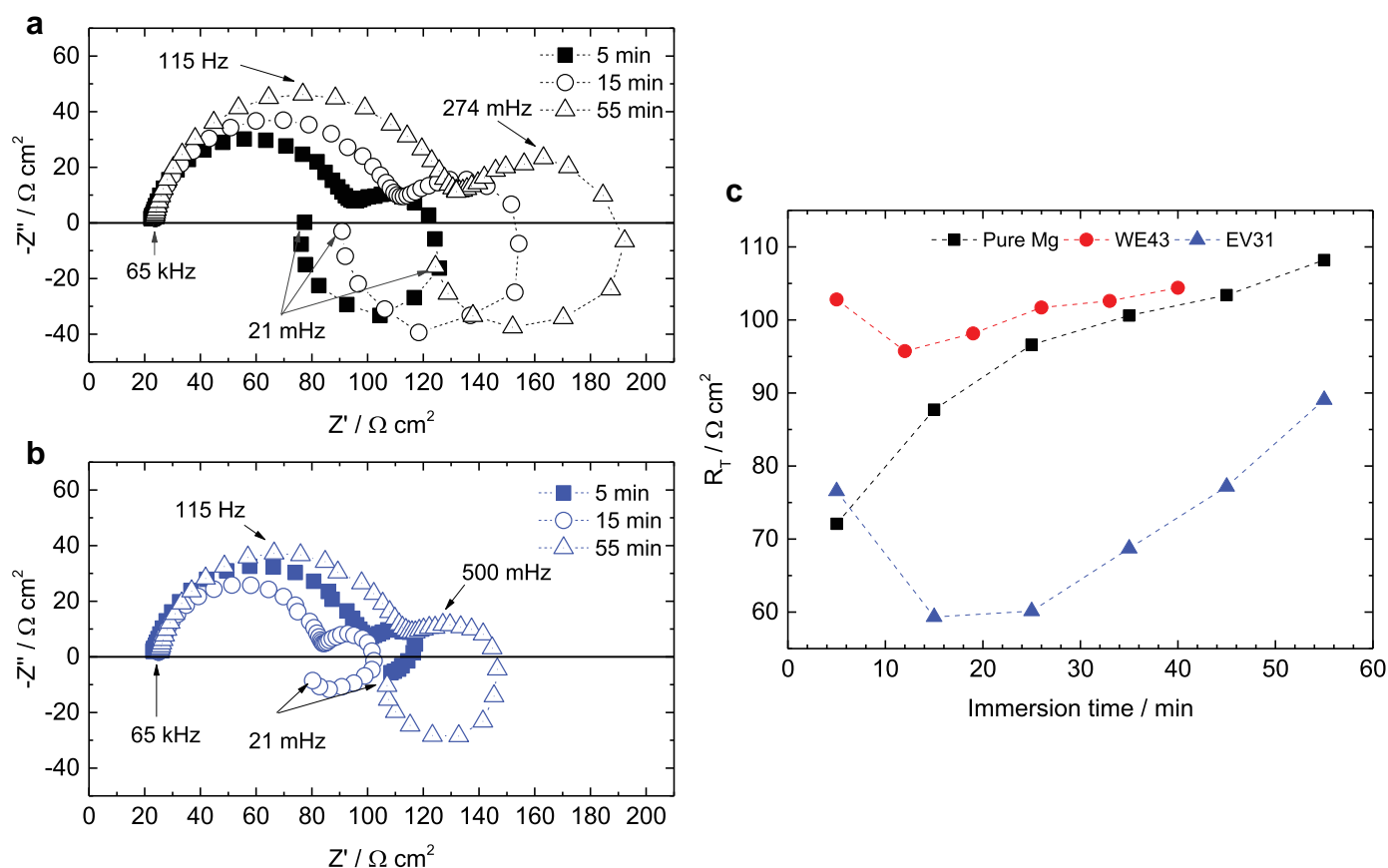


Fig. 7. Electrochemical impedance diagrams obtained for: (a) the pure Mg and (b) the EV31 Mg alloy for short immersion times; (c) Charge transfer resistance ( $R_T$ ) obtained for the pure Mg, the EV31 and the WE43 alloys from 5 min to 55 min of immersion in a 0.1M  $\text{Na}_2\text{SO}_4$  solution.

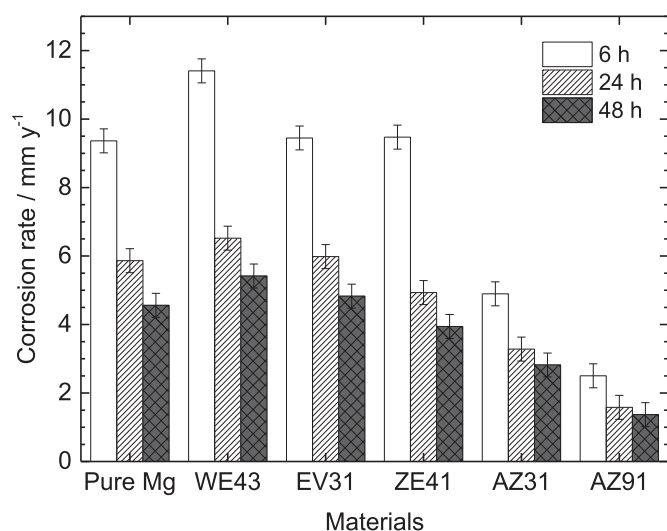


Fig. 8. Corrosion rates calculated from ICP-OES measurements (Eq. (1)) for the different Mg alloys and for the pure Mg after 6h, 24h and 48h of immersion in a 0.1M  $\text{Na}_2\text{SO}_4$  solution.

can be seen that a good agreement is obtained from the two procedures.

In order to compare the corrosion rates deduced from the electrochemical results with those obtained from the ICP-OES

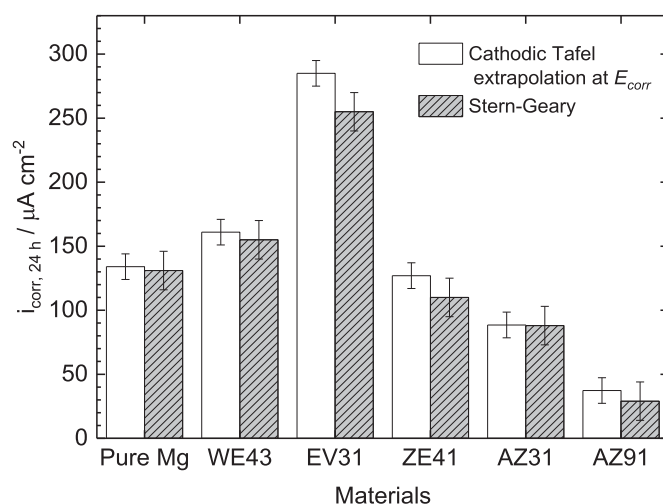


Fig. 9. Comparison of the instantaneous corrosion current densities for the Mg alloys and the pure Mg obtained from the extrapolation of the cathodic Tafel plot at  $E_{\text{corr}}$  (Fig. 3) or from the Stern-Geary relationship (Eq. (2)) after 24h of immersion in a 0.1M  $\text{Na}_2\text{SO}_4$ .

measurements, the mean corrosion current densities ( $i_{\text{corr},\text{mean}}$ ) were calculated from the Stern-Geary relationship (Eq. (5)) by using  $R_{T,\text{mean}}$  (Eq. (4)) and then, converted as corrosion rate (Eq. (6)). Fig. 10 compares the corrosion rates ( $\text{mm y}^{-1}$ )

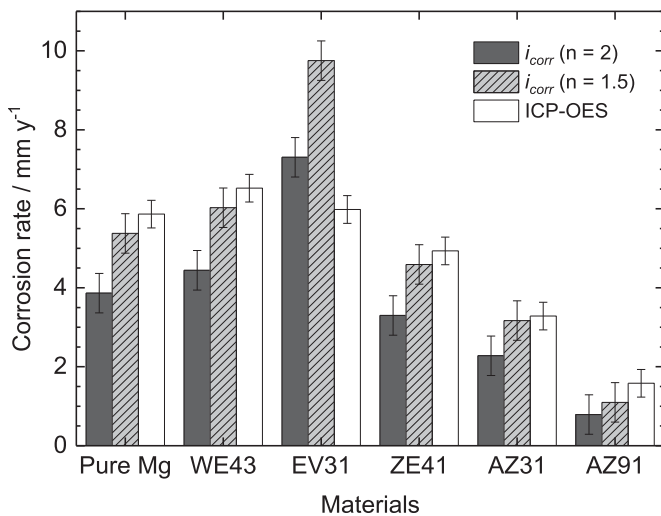


Fig. 10. Comparison of the mean corrosion rates of the Mg alloys and of the pure Mg during 24h of immersion in a 0.1M Na<sub>2</sub>SO<sub>4</sub> solution obtained from ICP-OES measurements (Eq. (1)) and from the electrochemical data based on the Stern-Geary relationship (Eq. 6 with  $n=2$  or  $n=1.5$ ).

calculated from the electrochemical results ( $i_{corr,mean}$ ) to those obtained from the ICP-OES measurements. First, it can be seen that the corrosion rates deduced from the electrochemical data by using a value of  $n=2$  are always lower than those determined from the ICP-OES analysis, except for the EV31 alloy. The use of a value of  $n=2$  led to an underestimation of the corrosion rates from the electrochemical measurements, as already reported [14,34–37]. A reason to explain the lower corrosion rates from the electrochemical results would be that, according to the corrosion mechanisms of Mg (reactions 1–5), the NDE would be due to a chemical reaction, which has no influence on the electrochemical results (reaction (3)). Thus, a value of  $n=1.5$  was considered to account for reaction (1) and for reactions (2) and (3) which are in parallel. By using a value of  $n=1.5$ , the quantity of Mg<sup>2+</sup> obtained from the electrochemical reaction (reaction (2)) is the same than that produced by the chemical reaction (reaction (3)). In that case, a perfect agreement was obtained between the corrosion rates determined from the ICP-OES analysis and those calculated from the electrochemical data (Fig. 10), except for the EV31 alloy. As it was shown in Fig. 7c, and in agreement with the high cathodic current densities (Fig. 4b), it can be assumed that for the EV31, the active surface area increased during the first hour of immersion and thus, the  $R_T$  values measured considering a geometrical surface area of 1 cm<sup>2</sup> were underestimated. Thus, the  $i_{corr,mean}$  value was overestimated. A variation of the surface area was also mentioned for the AZ91 after 72h of immersion (Fig. 6b) and attributed to an undermining effect.

It is noteworthy that the use of  $R_p$ , determined at the zero frequency on the impedance diagrams, instead of  $R_T$  in the Stern-Geary relationship would lead to similar conclusions because, as it can be seen in Fig. 5 and in Fig. 6, the  $R_p$  values are close to the  $R_T$  values.

The corrosion resistance ranking from the electrochemical results was the same than that obtained from the ICP-OES measurements and it confirmed that the two rare-earth Mg alloys have higher corrosion rates (2 to 3 times) than the AZ Mg alloys (Fig. 10). The corrosion rate of the ZE41 which contains lower rare-earth content was in between the EV31 and the AZ Mg series.

#### 4. Conclusions

The corrosion behaviour of five commercial Mg alloys was characterized by electrochemical techniques in a Na<sub>2</sub>SO<sub>4</sub> solution. The corrosion was controlled by two opposite effects: the dissolution of the Mg-rich matrix that mainly led to a progressive surface coverage by a protective film that decreased the active surface area and by the galvanic couplings between the intermetallic particles and the Mg matrix. The impedance diagrams primarily reflected the anodic dissolution of the matrix and the progressive formation of the oxides film. It was shown that the determination of the  $B$  coefficient from the current-voltage curves and for each alloy was necessary to determine the corrosion rates. Using only the impedance data could lead to wrong conclusions regarding their corrosion resistance. Finally, a good agreement was found between the corrosion rates determined from the ICP-OES analysis and the electrochemical data assuming the existence of two parallel paths in the corrosion mechanisms of Mg. The existence of a non-electrochemical reaction remains a possibility to explain the origin of the NDE. In the Na<sub>2</sub>SO<sub>4</sub> solution, the corrosion resistance of the rare-earth Mg alloys was lower than those of the Mg–Al alloys. For the EV31, a strong cathodic activity on the intermetallic particles and subsequently an increase of the active surface area led to an overestimation of its corrosion rate from the electrochemical data.

#### Acknowledgement

The authors gratefully acknowledge the IRT Saint-Exupery Surfinnov project partners, especially Mapaero and Prodem companies, for the financial support.

#### References

- [1] F. Czerwinski, *Corrosion Sci.* 86 (2014) 1–16.
- [2] C. Liu, S. Lu, Y. Fu, H. Zhang, *Corros. Sci.* 100 (2015) 177–185.
- [3] K. Gusieva, C.H.J. Davies, J.R. Scully, N. Birbilis, *Int. Mater. Rev.* 60 (2015) 169–194.
- [4] G.-L. Song, A. Atrens, X. Wu, B. Zhang, *Corrosion Sci.* 40 (1998) 1769–1791.
- [5] G.-L. Song, A. Atrens, M.S. Dargusch, *Corrosion Sci.* 41 (1999) 249–273.
- [6] R. Ambat, N.N. Aung, W. Zhou, *Corrosion Sci.* 42 (2000) 1433–1455.
- [7] G. Baril, C. Blanc, N. Pébère, *J. Electrochem. Soc.* 148 (2001) B489–B496.
- [8] S. Mathieu, C. Rapin, J. Steinmetz, P. Steinmetz, *Corrosion Sci.* 45 (2003) 2741–2755.
- [9] G. Baril, C. Blanc, M. Keddad, N. Pébère, *J. Electrochem. Soc.* 150 (2003) B488–B493.
- [10] G.-L. Song, A.L. Bowles, D.H. StJohn, *Mater. Sci. Eng. A* 366 (2004) 74–86.

- [11] A. Pardo, M.C. Merino, A.E. Coy, R. Arrabal, F. Viejo, E. Matykina, *Corrosion Sci.* 50 (2008) 823–834.
- [12] G. Galicia, N. Pèbère, B. Tribollet, V. Vivier, *Corrosion Sci.* 51 (2009) 1789–1794.
- [13] T. Zhang, Y. Li, F. Wang, *Corrosion Sci.* 48 (2006) 1249–1264.
- [14] G.-L. Song, A. Atrens, *Adv. Eng. Mater.* 5 (2003) 837–858.
- [15] N. Birbilis, M.A. Easton, A.D. Sudholz, S.M. Zhu, M.A. Gibson, *Corrosion Sci.* 51 (2009) 683–689.
- [16] A.D. Südholz, K. Gusieva, X.B. Chen, B.C. Muddle, M.A. Gibson, N. Birbilis, *Corrosion Sci.* 53 (2011) 2277–2282.
- [17] R. Arrabal, A. Pardo, M.C. Merino, M. Mohedano, P. Casajús, K. Paucar, G. Garcés, *Corrosion Sci.* 55 (2012) 301–312.
- [18] T. Takenaka, T. Ono, Y. Narazaki, Y. Naka, M. Kawakami, *Electrochim. Acta* 53 (2007) 117–121.
- [19] T.J. Luo, Y.S. Yang, Y.J. Li, X.G. Dong, *Electrochim. Acta* 54 (2009) 6433–6437.
- [20] H. Ardelean, A. Seyeux, S. Zanna, F. Prima, I. Frateur, P. Marcus, *Corrosion Sci.* 73 (2013) 196–207.
- [21] M. Ascencio, M. Pegguleryuz, S. Omanovic, *Corrosion* 87 (2014) 489–503.
- [22] P.-W. Chu, E.A. Marquis, *Corrosion Sci.* 101 (2015) 94–104.
- [23] A.E. Coy, F. Viejo, P. Skeldon, G.E. Thompson, *Corrosion Sci.* 52 (2010) 3896–3906.
- [24] F. Zucchi, V. Grassi, A. Frignani, C. Monticelli, G. Trabanelli, *J. Appl. Electrochem.* 36 (2006) 195–204.
- [25] S. Leleu, B. Rives, J. Bour, N. Causse, N. Pèbère, *Electrochim. Acta* 290 (2018) 586–594.
- [26] A. Kielbus, *J. Achiev. Mater. Manuf. Eng.* 22 (2007) 29–32.
- [27] P. Lyon, I. Syed, S. Heaney, *Adv. Eng. Mater.* 9 (2007) 793–798.
- [28] A.S. Hamdy, D.P. Butt, *Electrochim. Acta* 108 (2013) 852–859.
- [29] W.C. Neil, M. Forsyth, P.C. Howlett, C.R. Hutchinson, B.R.W. Hinton, *Corrosion Sci.* 51 (2009) 387–394.
- [30] M.-C. Zhao, M. Liu, G.-L. Song, A. Atrens, *Corrosion Sci.* 50 (2008) 3168–3178.
- [31] M.-C. Zhao, M. Liu, G. Song, A. Atrens, *Adv. Eng. Mater.* 10 (2008) 104–111.
- [32] R. Pinto, M.G.S. Ferreira, M.J. Carmezim, M.F. Montemor, *Electrochim. Acta* 56 (2011) 1535–1545.
- [33] G. Ben-Hamu, D. Eliezer, K.S. Shin, S. Cohen, *J. Alloys Compd* 431 (2007) 269–276.
- [34] A. Atrens, G.-L. Song, M. Liu, Z. Shi, F. Cao, M.S. Dargusch, *Adv. Eng. Mater.* 17 (2015) 400–453.
- [35] Z. Shi, M. Liu, A. Atrens, *Corros. Sci.* 52 (2010) 579–588.
- [36] A. Pardo, S. Feliu Jr, M.C. Merino, R. Arrabal, E. Matykina, *Int. J. Corros.* 2010 (2010) 7–13.
- [37] Z. Qiao, Z. Shi, N. Hort, N.I. Zainal Abidin, A. Atrens, *Corrosion Sci.* 61 (2012) 185–207.
- [38] A.D. King, N. Birbilis, J.R. Scully, *Electrochim. Acta* 121 (2014) 394–406.
- [39] L.G. Bland, A.D. King, N. Birbilis, J.R. Scully, *Corrosion* 71 (2015) 128–145.
- [40] V. Shkirskiy, A.D. King, O. Gharbi, P. Volovitch, J.R. Scully, K. Ogle, N. Birbilis, *ChemPhysChem* 16 (2015) 536–539.
- [41] J. Li, W. Sun, B. Hurley, A.A. Luo, R.G. Buchheit, *Corrosion Sci.* 112 (2016) 760–764.
- [42] S. Thomas, N.V. Medhekar, G.S. Frankel, N. Birbilis, *Curr. Opin. Solid State Mater. Sci.* 19 (2015) 85–94.
- [43] N. Birbilis, A.D. King, S. Thomas, G.S. Frankel, J.R. Scully, *Electrochim. Acta* 132 (2014) 277–283.
- [44] L. Rossrucker, A. Samaniego, J.-P. Grote, A.M. Mingers, C.A. Laska, N. Birbilis, G.S. Frankel, K.J.J. Mayrhofer, *J. Electrochem. Soc.* 162 (2015) C333–C339.
- [45] D. Höche, C. Blawert, S.V. Lamaka, N. Scharnagl, C. Mendis, M.L. Zheludkevich, *Phys.Chem.Chem.Phys* 18 (2015) 1279–1291.
- [46] M. Taheri, J.R. Kish, N. Birbilis, M. Danaie, E.A. McNally, J.R. McDermid, *Electrochim. Acta* 116 (2014) 396–403.
- [47] M. Curioni, *Electrochim. Acta* 120 (2014) 284–292.
- [48] S. Fajardo, C.F. Glover, G. Williams, G.S. Frankel, *Electrochim. Acta* 212 (2016) 510–521.
- [49] G.-L. Song, K.A. Unocic, *Corrosion Sci.* 98 (2015) 758–765.
- [50] G. Baril, G. Galicia, C. Deslouis, N. Pèbère, B. Tribollet, V. Vivier, *J. Electrochem. Soc.* 154 (2007) C108–C113.
- [51] M.P. Brady, G. Rother, L.M. Anovitz, K.C. Littrell, K.A. Unocic, H.H. Elsentriecy, G.-L. Song, J.K. Thomson, N.C. Gallego, B. Davis, *J. Electrochem. Soc.* 162 (2015) C140–C149.
- [52] M. Taheri, M. Danaie, J.R. Kish, *J. Electrochem. Soc.* 161 (2014) C89–C94.
- [53] S. Fajardo, G.S. Frankel, *Electrochim. Acta* 165 (2015) 255–267.
- [54] G.S. Frankel, S. Fajardo, B.M. Lynch, *Faraday Discuss.* 180 (2015) 11–33.
- [55] A. Samaniego, B.L. Hurley, G.S. Frankel, *J. Electroanal. Chem.* 737 (2014) 123–128.
- [56] G. Baril, N. Pèbère, *Corrosion Sci.* 43 (2001) 471–484.
- [57] B.A. Boukamp, *J. Electrochem. Soc.* 142 (1995) 1885–1894.
- [58] M. Stern, A.L. Geary, *J. Electrochem. Soc.* 104 (1957) 56–63.
- [59] V. Angelini, I. Boromei, L. Ceschini, A. Morri, *La Metall. Ital.* 9 (2015) 37–42.
- [60] A. Kielbus, T. Rzychon, R. Przeliorz, *Mater. Sci. Forum* 638–642 (2010) 1447–1452.
- [61] B. Moulis, L. Arurault, P.-L. Taberna, C. Bonningue, *J. Magnes. Alloys* 2 (2014) 363–376.
- [62] N. Pèbère, C. Riera, F. Dabosi, *Electrochim. Acta* 35 (1990) 555–561.
- [63] A.D. Südholz, N.T. Kirkland, R.G. Buchheit, N. Birbilis, *Electrochem. Solid-State Lett* 14 (2011) C5–C7.
- [64] D.S. Gandel, M.A. Easton, M.A. Gibson, T. Abbott, N. Birbilis, *Corrosion Sci.* 81 (2014) 27–35.
- [65] N. Hara, Y. Kobayashi, D. Kagaya, N. Akao, *Corrosion Sci.* 49 (2007) 166–175.
- [66] K.A. Unocic, H.H. Elsentriecy, M.P. Brady, H.M. Meyer, G.L. Song, M. Fayek, R.A. Meisner, B. Davis, *J. Electrochem. Soc.* 161 (2014) C302–C311.